ISSN 0027-1349, Moscow University Physics Bulletin, 2018, Vol. 73, No. 6, pp. 659–668. © Allerton Press, Inc., 2018.
Original Russian Text © R.V. Zakharov, V.V. Shorokhov, A.S. Trifonov, R.B. Vasiliev, 2018, published in Vestnik Moskovskogo Universiteta, Seriya 3: Fizika, Astronomiya, 2018, No. 6, pp. 00000–00000.

CONDENSED MATTER PHYSICS

The Transport of Electrons through Tetrapod-Shaped CdTe/CdSe Nanocrystals

R. V. Zakharov[a, b, *], **V. V. Shorokhov**[a, e], **A. S. Trifonov**[b, e, f], and **R. B. Vasiliev**[c, d]
[a] *Department of Physics, Moscow State University, Moscow, 119991 Russia*
[b] *Scobeltsyn Institute of Nuclear Physics, Moscow State University, Moscow, 119991 Russia*
[c] *Department of Material Science, Moscow State University, Moscow, 119991 Russia*
[d] *Department of Chemistry, Moscow State University, Moscow, 119991 Russia*
[e] *Quantum Technology Center, Moscow State University, Moscow, 119991 Russia*
[f] *Kotel'nikov Institute of Radioengineering and Electronics, Russian Academy of Sciences,*
ul. Mokhovaya 11/7, Moscow, 125009 Russia
**e-mail: zakharov.ru14@physics.msu.ru*

Received March 27, 2018; in final form, May 10, 2018

Abstract—A quasi-one-dimensional model was developed for the transport of electrons in the scanning tunneling microscope needle—CdTe/CdSe tetrapod-shaped nanocrystal system. This model was used as a basis to study the effect of the concentration of charge carriers in the tetrapod and its energy band structure, the geometry, and the spatial orientation with respect to the substrate on the voltage—current characteristics. The major classes of voltage—current characteristics that could be experimentally measured were determined by numerical modeling. The thus-determined classes of voltage—current characteristics were immediately related with the spatial orientation and sizes of tetrapods. This classification of voltage—current characteristics was used to separate the voltage—current characteristics, which corresponded to the transport of electrons from the scanning microscope needle through the tetrapod into the substrate, from the array of previously measured characteristics. The numerically calculated and experimental characteristics were compared with each other to determine the best-fit parameters of this model.

Keywords: tetrapods, tunnel effect, nanocrystals, electron transport, voltage—current characteristic.

DOI: 10.3103/S0027134918060267

INTRODUCTION

Semiconductor crystals with characteristic sizes from several nanometers to several tens of nanometers and a complicated spatial structure and atomic composition are characterized by rather unusual size-dependent optical and electrical properties, which are governed by the effects of the tunneling of electrons and the size quantization of their electron energy spectrum [1–5]. High-quality nanocrystals with a nearly ideal atomic structure are synthesized by the methods of colloid chemistry [6–11]. Semiconductor crystals can be used as a functional material for the elements of nanoelectronics and photovoltaics and the creation of metamaterials [12–14].

One of the interesting classes of semiconductor nanostructures is branched nanoparticles, e.g., tetrapods [15, 16], octopods [17], and hyperbranched nanoparticles [18]. In the works on such nanocrystals, great scientific interest exists in studying the properties of electrical conductivity in branched tetrapod nanocrystals by both theoretical and experimental methods [16, 19–21]. Tetrapod-shaped nanoparticles consist of four rays linked at a tetrahedral angle $\varphi = 100°–110°$ in the central point. Tetrapods can have a homogeneous chemical composition or consist of several different areas. One distinctive feature of such nanocrystals is a high ratio of the number of surface atoms to their total number (>20%). Due to their shape and great number of surface atoms, tetrapods can be used to construct optoelectronic devices, e.g., solar batteries [13, 22], light-emitting diodes, and single-electron devices with several active charge centers [19].

One of the methods used for the experimental characterization of tetrapod-shaped nanocrystals is to study the properties of their electrical conductivity. For this purpose, the voltage—current characteristics of individual particles immobilized on the surface of a conducting substrate are experimentally measured with a scanning tunneling microscope (STM) [21]. Such a method was used in the previous works in the experimental study of isolated CdTe and CdTe/CdSe tetrapod-shaped nanoparticles [20] on a surface of gold and titanium [21]. As a result of these works, the question of how tetrapod-shaped crystals on the surface of a conducting substrate can be identified from

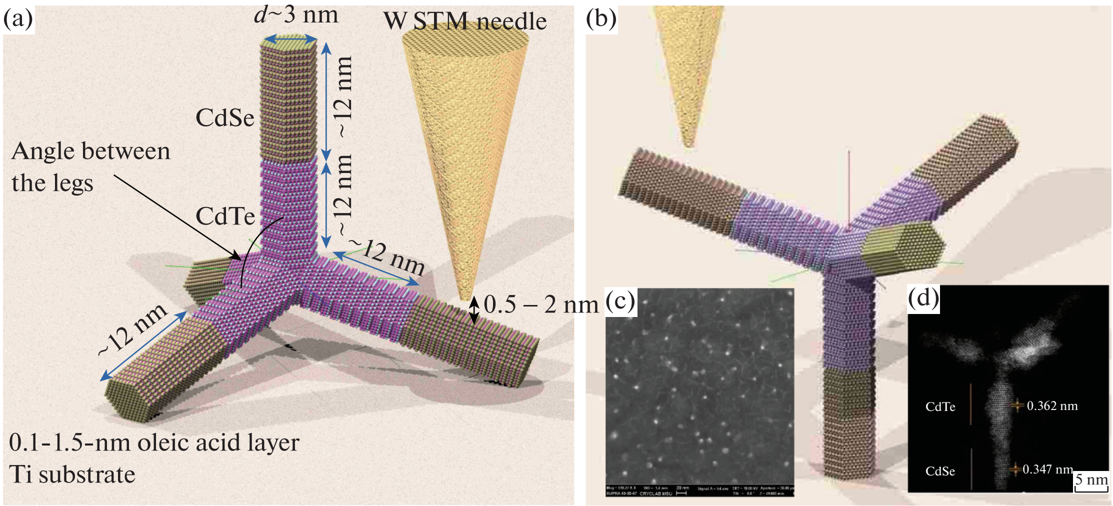

Fig. 1. The spatial structure of a model ideal CdTe/CdSe tetrapod, whose leg is oriented (a) upwards and (b) downwards, on the surface of a crystalline substrate with the metallic STM needle tip, which is schematically shown in the (a) right and (b) left upper corner and (c) SEM and (d) TEM photos of real CdTe/CdSe tetrapods on a crystalline substrate.

STM data has remained open. For this reason, the theoretical study of the transport of an electrical charge through isolated nanoparticles is of both fundamental and great practical interest [19, 23, 24].

In this work, a quasi-one-dimensional model of the transport of electrons through isolated CdTe/CdSe tetrapod-shaped nanocrystals was developed and the properties of their electrical conductivity were studied by numerical calculation.

1. MODEL OF THE CONSIDERED SYSTEM

The properties of electrical conductivity in isolated CdTe/CdSe tetrapod-shaped nanocrystals were studied by developing a physical model that incorporate the following components: a conducting substrate, an oleic acid monolayer, a CdTe/CdSe tetrapod-shaped nanocrystal, a vacuum tunneling barrier, and a STM needle. The spatial structure of the model ideal CdTe/CdSe tetrapod located on the surface of a solid-state substrate is shown in Fig. 1a. The experimental photos taken of tetrapods with the use of scanning and transmission electron microscopes (SEM and TEM) are shown in Figs. 2b and 2c [20]. A detailed consideration of this system is given in Appendix 1.

The major part of the model calculations were performed at a model temperature of $T = 300$ K. Some voltage–current curves (VCCs) were calculated using a model temperature close to absolute zero $T = 0$ K to provide a better presentation for the microstructure of their current steps.

This work was performed using the phenomenological quasi-classic approximation, in which the conduction-band electron and the valence-band holes were considered as a certain liquid. In such an approximation, the electron or hole density may vary and redistribute in the volume of a tetrapod under an external electrical field by any elementary charge fraction. Such a redistribution is understood to mean the polarization and probabilistic redistribution of the charge of corresponding carriers, which satisfy the condition of normalization to the total charge

$$\int\limits_V \rho_e(\mathbf{r})dV = Q_e, \quad \int\limits_V \rho_p(\mathbf{r})dV = Q_p. \tag{1}$$

Such an approach provides the ability to use the quasi-classic transport equations to determine the equilibrium electron density distribution inside the volume of a tetrapod depending on the applied external electrical field.

To determine the initial electron and hole density distribution, the concentration of the intrinsic charge carrier, conduction-band electrons, and valence-band holes was estimated. The concentration of these carriers was estimated by the formula

$$n_e = \int\limits_{E_e}^{\infty} f(E,T)\frac{dN}{dE}dE, \quad n_p = \int\limits_{-\infty}^{E_v} f(-E,T)\frac{dN}{dE}dE, \tag{2}$$

where E_c and E_v are the conduction band bottom and the valence band top, respectively, $f(E, T)$ is the Fermi distribution function, and dN/dE is the density of states. The concentration of intrinsic charge carriers was neglected in this work.

The energy band diagram of this structure is shown in Fig. 2, where the z axis is always oriented along one of the legs of the tetrapod, i.e., it has an inflection in the center. This leads to a kink in the diagram profile in the center of the tetrapod, as the projection of the field is changed after the leg is turned around. The conduction band of CdTe is higher than for CdSe; thus, a second barrier is formed inside the tetrapod.

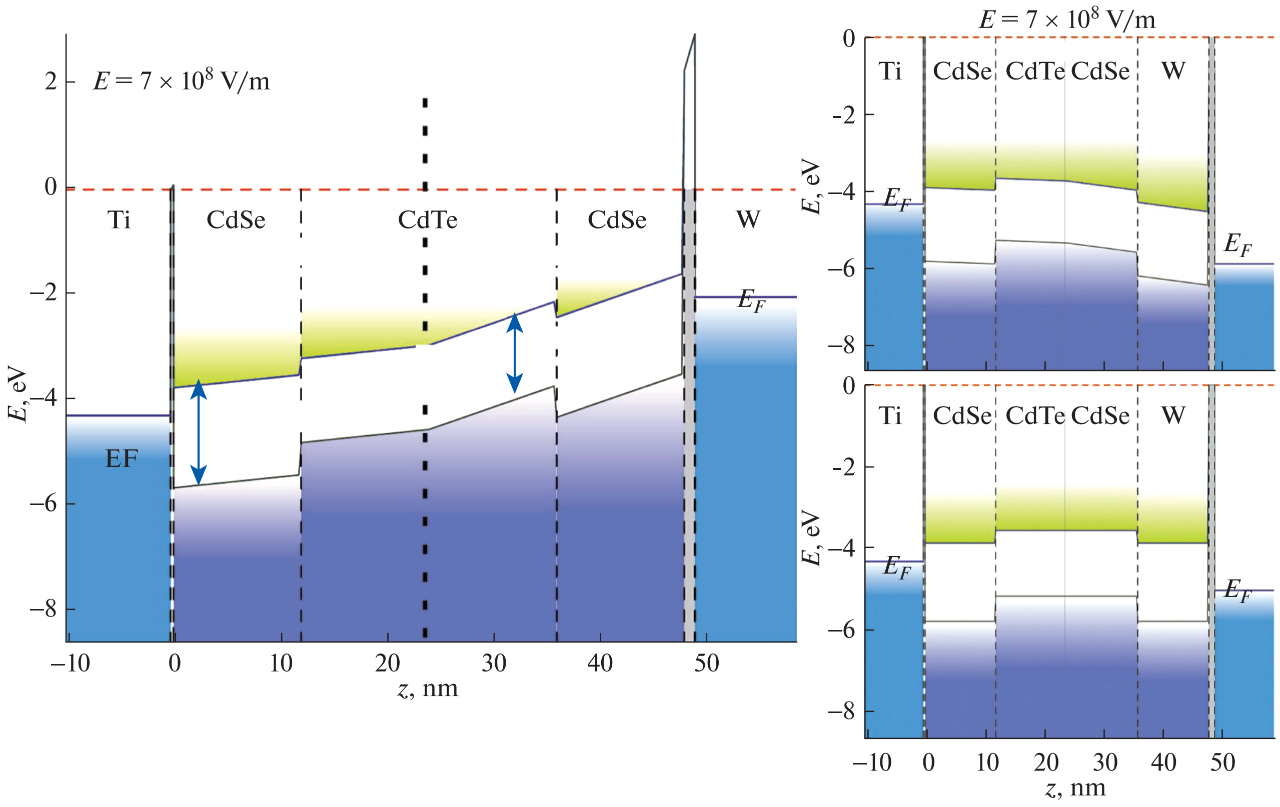

Fig. 2. The energy band diagram at a positive external field (left), a reverse polarity (right), and zero field (bottom right).

This barrier disappears at a rather high voltage, thus producing an effect on the voltage–current characteristics of the tetrapod.

The change in the concentration of free charge carriers (holes and electrons) at a certain external field E is described by the following self-consistent equations [25–27]:

$$\frac{\partial n}{\partial t} = \mu_n\left(E\frac{\partial n}{\partial z} + n\frac{\partial E}{\partial z}\right) + D_n\frac{\partial^2 n}{\partial z^2} + G_n - \frac{n - n_0}{t_n},$$

$$\frac{\partial p}{\partial t} = -\mu_p\left(E\frac{\partial p}{\partial z} + n\frac{\partial E}{\partial z}\right) + D_p\frac{\partial^2 n}{\partial z^2} + G_p - \frac{p - p_0}{t_p}, \quad (3)$$

where n and p are the concentrations of holes and electrons, μ_n and μ_p are their mobilities, D_n and D_p are their diffusion coefficients, G_n and G_p are their generation rates, and t_n and t_p are their characteristic recombination times.

We assume that the electron transport process has a ballistic character. The model of the relaxation of carriers due to scattering processes can be used as a further improvement of our model.

The transmission factor of the potential tetrapod structure were calculated by the method of the transport matrix [28]

$$\begin{pmatrix}\Psi^+_{j+1}\\ \Psi^-_{j+1}\end{pmatrix} = \frac{1}{2}\begin{pmatrix}1+\alpha_j & 1-\alpha_j\\ 1-\alpha_j & 1+\alpha_j\end{pmatrix} \times \begin{pmatrix}2^{i(k_j-k_{j+1})\Delta z} & 0\\ 0 & 2^{-i(k_j-k_{j+1})\Delta z}\end{pmatrix}\begin{pmatrix}\Psi^+_j\\ \Psi^-_j\end{pmatrix}, \quad (4)$$

where $\alpha_j = \dfrac{k_j}{k_{j+1}}$, $k_j = \sqrt{\dfrac{2m^*_j(E_{el} - U_j)}{\hbar^2}}$, and m^*_j is the effective mass of an electron. The probability of tunneling through the tetrapod structure (transmission) is the ratio of the incident flux to the transmitted flux $T = \dfrac{j_N}{j_0} = \dfrac{k_N|\Psi^+_N|^2}{k_0|\Psi^+_0|^2}$.

The tunneling conductivity was calculated by the Landauer formula (following from the Tsu–Esaki formula at a constant density of lateral modes [29]):

$$G = \frac{2e^2}{h}\frac{dn_\perp}{dE}\int_{-\infty}^{\infty} T(\varepsilon)(f(\varepsilon) - f(\varepsilon + eV_T))d\varepsilon, \quad (5)$$

where $\dfrac{dn_\perp}{dE}$ is the density of laterally quantum modes, $f(\varepsilon)$ is the Fermi–Dirac distribution at a corresponding temperature, and $T(\varepsilon)$ is the structure transmission. The current is found via the numerical integration of the conductivity taking the fact that $I(V_T = 0) = 0$ into account.

2. RESULTS AND DISCUSSION

2.1. *Perturbation of the Field by Charge Carriers*

If a certain external field E is specified and the current concentrations of electrons (n) and holes (p) are known, it is necessary to solve the Poisson equation $\epsilon\epsilon_0\Delta\varphi = (n - p)e$, where e is the dielectric permittivity of the medium, to calculate the effective field in which mobile charge carriers reside. Assuming that the tetrapod leg is approximately a cylinder with a radius R, it is possible to pass to the quasi-one-dimensional distribution of the electrical field. Let us orient the Z axis along the leg. Then, the potential at the point z_0 from the element with a thickness h (along the Z axis) at the point z_i, i.e., at a distance $\Delta z_i = |z_0 - z_i|$ is

$$\varphi_0^i(\Delta z_i, h, r) = \int_0^h dh \int_0^R dr \frac{1}{4\pi\epsilon_0}\frac{\rho_i(r)2\pi\Delta z_i r}{\sqrt{r^2 + \Delta z_i^2}}, \qquad (6)$$

where ρ is the bulk charge density (C/m^3). Assuming that the tetrapod charge is uniformly distributed over the cross section of a leg, the contribution to the electrical field at the point z_0 from the element, which has a thickness h and is located at the point z_i, is

$$\Delta E(\Delta z_i) = -\frac{2\pi\rho}{4\pi\epsilon\epsilon_0} \\ \times ((\sqrt{(\Delta z_i + h)^2 + R^2} - \Delta z_i - h) - (\sqrt{\Delta z_i^2 + R^2} - \Delta z_i)). \qquad (7)$$

The resulting vector of the electrical field intensity in the element z_0 is

$$E(z_0) = \sum_{i=1}^{n} \Delta E(\Delta z_i) sign(z_0 - z_i). \qquad (8)$$

The considered tetrapod consists of four legs. The field from a certain leg can be calculated in the above described one-dimensional model and the field projection onto the Z axis on a certain leg from the other leg will be calculated assuming that the elements of the other leg are point charges. Since the angles between the legs and the surface are small $\alpha = (4°–19°)$, the field from the other legs on a certain leg will be small and the inaccuracy of such a calculation is not essential.

2.2. *The Tunneling Current*

To calculate the electrical current through the tetrapod, the intensity of the external electrical field E_0 was specified at the first stage. Equation (3) was solved by the explicit difference scheme. The self-consistent field was calculated according to the method described in Section 2.1. The recurrent procedure was further used to determine the steady-state distribution of charge carriers via the comparison of carrier distributions at sequential calculation steps. The effective electrical potential along the system axis was calculated from the steady-state electrical charge distribution in the tetrapod.

The established concentrations of carriers at certain external fields, the effective energy profile, and the electrical field contribution are shown in Figs. 3a, 3b, and 3c, respectively. Since the concentrations and field profiles in three legs adjacent to the substrate are the same due to symmetry, all the profiles are plotted along the Z axis with an inflection in the tetrapod center (i.e., the Z axis passes through the symmetry axis of one of the legs adjacent to the substrate and through the symmetry axis of the upper leg). It can be seen that charge carriers are generally concentrated at the boundaries of the zones. However, the concentrations of carriers in the considered structure are 10^{17} cm^{-3} and do not introduce any appreciable change to the electrical potential. Considerable distortions will occur in the potential profile at concentrations that are increased by 100 times.

The effective potential profile and the transport matrix method (Eq. (4)) were used to calculate the structure transmission $T(\varepsilon)$ for different electron energies. The energy step was dynamically varied, as the dependence $T(\varepsilon)$ is nonlinear and has resonance peaks. Immediately after the relative change T exceeded 20% at a certain step, the energy was taken equal to the energy at the previous step and the energy step was decreased by two times, while if the relative change was less than 5% the energy step was increased by two times. The current was then calculated by the Landauer formula (Eq. (5)) with numerical integration. To improve the precision of calculations near $T(\varepsilon)$ resonances, the method described in Section 2.3 was developed.

To estimate the change in the concentrations of charge carriers inside the tetrapod in the process of their transport it is necessary to determine the density of lateral quantum modes (see Appendix 1), which lie between the substrate and STM needle chemical potentials. In addition, to estimate the possibility of the concentration of charge carriers inside the tetrapod, we assume that the internal structure of the tetrapod is ideal, i.e., it does not have any crystal lattice defects and admixtures. The number of such modes and the transmissions of barriers provide the ability to estimate the flux of arriving and departing electrons. The total number of states inside the tetrapod can be estimated as

$$n = \frac{2m^* SeV_T}{\pi\hbar^2}\sum_{a_\perp}\Delta n_\parallel(n_\perp, V_T), \qquad (9)$$

which at a voltage of 1 V gives the estimate $n \sim 200$ for the total number of states for charge carriers within an energy range from the conduction band bottom to the substrate or STM needle chemical potential.

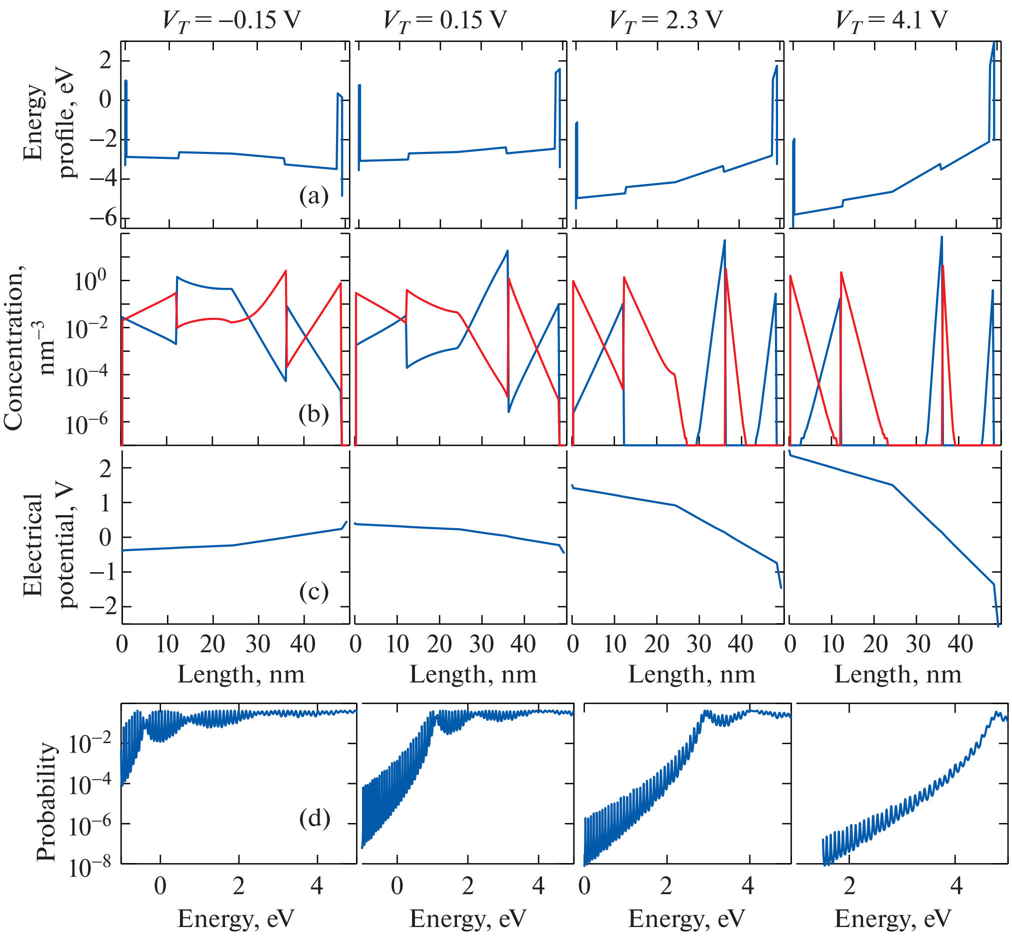

Fig. 3. (a) The effective potential, (b) concentration of holes (blue) and electrons (red), and (c) electrical potential versus tetrapod longitudinal coordinate (this axis is curves and passes along one of the three legs and then along the central leg and (d) probability of tunneling through the tetrapod versus electron energy at four voltage differences of −1.5, 0.15, 2.3, and 4.1 V.

2.3. Correction for the Resonant Transmission Behavior

The dependences of the transmission T on the electron energy E (Fig. 3d) can be seen to have a kink: electrons pass over the CdTe barrier at this energy. Periodic narrow peaks, which attain 1 and can be approximated by the Breit–Wigner formula for the structure with one or two quantum wells [30, 31], can also be observed. These are associated with the quasi-steady states formed due to the resonant states of electrons between the substrate and STM needle tunneling barriers. Assuming that the Fermi–Dirac distribution is almost constant near a peak, it is possible to derive the analytical expression of integral (5) near the peaks:

$$\int_{E_{peak}-\delta E}^{E_{peak}+\delta E} T(E)dE = \frac{2}{\sqrt{k}}\arctan\sqrt{k}\delta E. \tag{10}$$

As can be seen from Fig. 3d, the numerical calculation of $T(\varepsilon)$ peaks did not bring them to 1, even with a dynamic step, as they are very narrow. The behavior of the T peaks can be described by the Breit–Wigner formula $T(\varepsilon) = \dfrac{\Gamma^2}{\Gamma^2 + (\varepsilon - \varepsilon_{peak})^2}$. The existence of a peak is possible in the regions where T becomes strongly nonlinear (the energy step appreciably decreases). To perform the precise identification of a peak, the dependence $\ln T$ @ $\ln(\varepsilon - \varepsilon_{peak})$ was plotted at $T \ll 1$. If this dependence is linear and the coefficient calculated by the least-squares technique is -2 ± 0.1, it is really transmission resonance. Most of the candidates for being classified as peaks satisfied this condition; however, the coefficient calculated for the others by the least-squares technique strongly deviated from 2.

It was revealed that transmission peaks make the most appreciable contribution to the conductivity, i.e., the current occurs predominantly due to the resonant tunneling between the substrate and the STM needle.

The major difficulty in the consideration of such a structure is that the quasi-one-dimensional method is used to calculate the transmission of the potential structure of a tetrapod without incorporating the

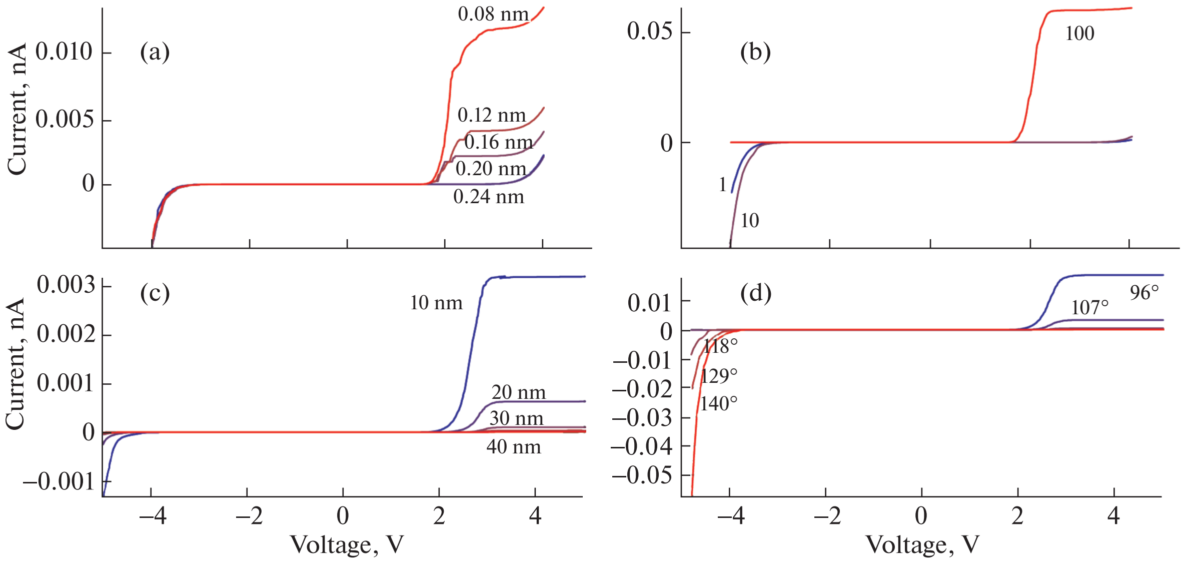

Fig. 4. Current versus voltage at a change in different parameters at the first (blue) and second (red) limits and current versus (a) oleic acid monolayer thickness ranged from 0.24 to 0.08 nm with a step of 0.04 nm, (b) concentration increased by 1, 10, and 100 times, (c) central CdTe part length varied from 10 to 40 nm with a step of 10 nm, and (d) interleg angle varied from 96° to 140° with a step of 11° at a temperature $T = 0$ K.

branching point into such calculation. The quasi-one-dimensional model of a tetrapod with 3 legs is considered in Appendix 3.

2.4. Analysis of the Voltage–Current Characteristics and Comparison with an Experiment

The current was theoretically calculated and experimentally measured in the system whose model is
1 described in Section 2 and schematized in Fig. 2, including a substrate, an oleic acid layer, a tetrapod, and an STM needle.

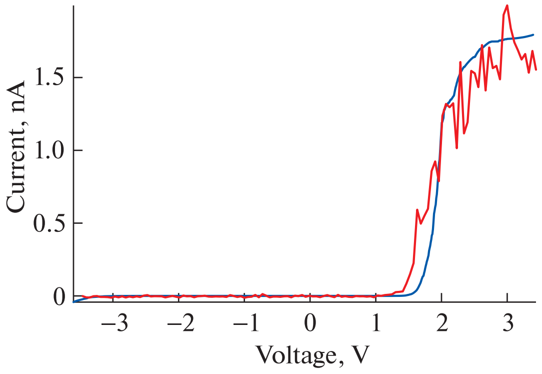

Fig. 5. The calculated (blue) and STM measured (red) voltage–current characteristics. The parameters of the calculation: tunneling gap between the STM needle and the tetrapod, 1 nm; oleic acid monolayer thickness, 0.28 nm; length of CdSe/CdTe/CdSe tetrapod legs, 12/24/12 nm; electron and hole concentration, 10^{17} cm^{-3} and 10^{16} cm^{-3} in CdSe; 10^{17} cm^{-3} and 5×10^{17} cm^{-3} in CdTe, respectively. The parameters of the measurement: tunneling voltage, 300 mV; tunneling current, 0.2 nA.

All the calculated plots (Fig. 4) contain a step that has a length of ~0.5–1 V and occurs at a voltage of 2–6 V in both the forward and backward directions (the differential conductivity abruptly decreases in this case). However, rapid nonlinear growth in the current occurs both before and after the step. At great magnification, it is possible to see small stepped current jumps that occur due to the resonant tunneling of electrons.

The oleic acid barrier value has an effect on the location of this step (the lower the barrier is, the sooner this step occurs). In a similar way, it has been established that the vacuum barrier thickness also has an effect on the location of this step in the backward direction.

The effect of the concentration of intrinsic carriers on the shape of VCC plots has also been determined in the plot (Fig. 4b). It has been established that the shape of this plot undergoes an appreciable transformation only when the concentrations of carriers are increased to 10^{19} cm^{-3}. The tetrapods used in the experiments were not specially doped and the concentrations of free charge carriers in them were less than 10^{17} cm^{-3}.

The length of CdTe legs (varied within a range of 10–50 nm) has a slight effect on the shape of VCCs (Fig. 4c), but appreciably changes the current amplitude.

The angle in an ideal tetrapod is tetrahedral, but the tetrapod leg may bend under an electrostatic field [32]. It has been revealed that the angle between

CdSe/CdTe tetrapod legs has an effect of the symmetry of VCCs (Fig. 4d). At angles close to 90°, the conductivity at a positive field is several orders of magnitude higher. At 130°, the voltage–current characteristic is nearly symmetric. The symmetry of plots also depends on the thickness of barriers; however, this dependence is not very strong.

The calculated VCCs were compared with previous experimental results [21]. The measured and calculated VCC for the needle located just above the upper leg are shown in Fig. 5 at the parameters specified in the figure caption.

CONCLUSIONS

A quasi-one-dimensional model of the transport of electrons through the nanocrystals of CdSe/CdTe tetrapods has been developed in this work. The model was used as a basis to study the dependence of the properties of electrical conductivity in the nanocrystals of CdTe/CdSe tetrapods on their geometric parameters (the length and radius of the legs and the tetrahedral angle), the concentration of charge carriers, the spatial orientation with respect to the crystalline substrate, and the width of the oleic and vacuum tunneling barriers.

It has been established that the concentration of charge carriers in a tetrapod has almost no effect on the shape of the dependence of the electrical conductivity on the applied bias voltage under normal conditions that correspond to a real experiment. Nevertheless, an increase in the concentration of charge carriers by 100 times in comparison with its normal level already appreciably changes the shape of the dependence of the electrical conductivity on the applied voltage due to the occurrence of additional Coulomb barriers in the regions where charge carriers are concentrated.

It has been revealed that the tetrahedral angle value is crucial for the symmetry of voltage–current characteristics. When the angle between the legs is close to $\varphi = 90°$, the currents at one voltage are several orders of magnitude greater than at a reverse voltage.

At low temperatures, the voltage–current characteristics of a CdTe/CdSe tetrapod-shaped nanocrystal contain a great number of small current steps at different bias voltage scales; their existence can be explained by the additional reflections on heterojunctions, near which additional local tunneling barriers and potential wells are formed.

A characteristic feature of the voltage–current characteristics of CdTe/CdSe tetrapods is the existence of a large-scale current step in the region of positive bias voltages from 2 to 5 V. When the bias voltage is higher than this threshold value, the current almost ceases to grow within a range of nearly 0.5–1 V. The crucial factor for the location of such a step is the width of tunneling barriers formed by oleic acid on the surface of the substrate and the vacuum gap between the STM needle and the tetrapod-shaped nanocrystal. This step can be used for the unique identification of tetrapod nanocrystals on substrates during their STM study. Among the great variety of the previously measured voltage–current characteristics of CdTe/CdSe tetrapod-shaped nanocrystals, a great number of experimental curves with such characteristic steps were revealed by STM methods.

The voltage–current characteristics obtained by numerical calculation agree with the available experimental data with a good degree of precision.

3. ADDITIONAL MATERIALS

3.1. Appendix 1. A Detailed Description of the Studied System

Conducting gold and titanium substrates were used as a substrate in the experiments [21]. In the proposed model, the substrate material is taken into account with the use of model parameters, such as the Fermi level position $E_{F,\,\mathrm{sub}}$ and the near-surface density of electron states ρ_{el}. The model values of Fermi level positions for these materials were determined from the tabular data as $E_{F,\,\mathrm{Au}} = 4.3$ eV and $E_{F,\,\mathrm{Ti}} = 3.95$ eV.

The oleic acid monolayer creates the tunneling barrier between the substrate and the tetrapod. The spatial width of such a tunneling barrier in the proposed model is equal to the oleic acid monolayer width, and the energy height is determined as the difference between the lowest unoccupied molecular orbital (LUMO) position for the closely packed molecular layer and the metal Fermi level. In the experiments in [21], the oleic acid layer was necessary to immobilize tetrapod crystals on the substrate surface in the atmosphere. The model parameters selected for the oleic acid monolayer were the monolayer width L_A and the relative dielectric permittivity ε_A. The tabular data $\varepsilon_A = 2.46$ were taken for the relative dielectric permittivity. The thus-determined dielectric permittivity must take the effect of polarization between acid molecules in the external electrical field created by the STM needle into account. The width of the oleic acid monolayer was varied in calculations within a range $L_A = 0.1$–1.5 nm.

Heterojunction tetrapods, whose central part consists of CdTe and has a wurtzite-type crystal structure, and whose leg tips consist of CdSe and have a sphalerite-type structure, were studied in this work. The geometric characteristics of a CdTe/CdSe tetrapod nanocrystal strongly depend on the method of its synthesis and conditions of its growth. Among its principal characteristics are the tetrahedral angle between the legs φ, the radius of the legs R, the total length of the legs L, and the length of tetrapod leg components L_{CdTe} and L_{CdSe}, which meet the condition

$$L = L_{\mathrm{CdTe}} + L_{\mathrm{CdSc}}. \tag{11}$$

Table 1. The estimated number of electron and hole states per unit volume dN_e/dV and dN_p/dV and unit leg length dN_e/dz and dN_p/dz for different CdSe/CdTe tetrapod parts

Tetrapod part	dN_e/dV	dN_p/dV	dN_e/dz	dN_p/dz
CdSe	10^{17}–10^{18} cm^{-3}	10^{17}–5×10^{17} cm^{-3}	0.001–0.01 nm^{-1}	0.001–0.005 nm^{-1}
CdTe	10^{17}–5×10^{17} cm^{-3}	10^{17}–5×10^{17} cm^{-3}	0.001–0.005 nm^{-1}	0.001–0.005 nm^{-1}

Table 2. The effective mass (m^*) and mobility (μ) of electrons and holes and relative dielectrical permittivity in different CdTe/CdSe tetrapod parts

Tetra-pod part	m_e^*	m_h^*	μ_e	μ_p	ϵ
CdSe	$0.13m_e$	$0.45m_e$	620 cm^2 (V s)$^{-1}$	14 cm^2 (V s)$^{-1}$	10
CdTe	$0.13m_e$	$0.35m_e$	1200 cm^2 (V s)$^{-1}$	50 cm^2 (V s)$^{-1}$	10
Oleic acid					2.34

The total model length of the legs was varied within a range $L = 20$–150 nm. The basic value taken in this work for these components is $L_{\text{CdTe}} = L_{\text{CdSe}} = 12$ nm, which corresponds to the real experimental situation [15, 16, 20, 33]. The properties of electrical conductivity in CdTe/CdSe tetrapods were also studied in this work depending on their orientation with respect to the substrate. Three possible orientations were considered, that is, where the tetrapod is supported by three legs, the tetrapod is turned around and supported by two legs, and the tetrapod is turned upside down and supported by one leg. It should be noted than the tetrapod legs that contact the substrate are equivalent to each other with respect to their turning, respectively, around the third- and second-order axes perpendicular to the substrate in the first two cases; this was taken into account in the numerical calculation of the voltage–current characteristics.

In the general case, the radius of the legs can gradually change from the tetrapod center to the leg tips as required by the specified function $R(z)$, where z is the coordinate along a tetrapod leg. In this work, the radius change along a leg was not taken into account and the radius of a leg was assumed to be constant throughout its entire length, but can be varied as a model parameter. The range of the radii of tetrapod legs was specified as $R = 1.0$–3 nm. Tetrapod nanocrystals may also have more complicated geometric configurations with bent legs due to mechanical stress [32]. Such a bent configuration unavoidably complicates the shapes of the effective potential, in which an electron move in a tetrapod.

A second tunneling barrier, whose width is governed by the operational regime of a scanning tunneling microscope and may attain $L_{\text{vacuum}} = 0.5$–3 nm, is formed between the STM needle and the tetrapod. The height of this tunneling barrier is determined by the position of the Fermi level of STM needle with respect to the continuum.

For a tetrapod with a total length of one leg $L = 24$ nm and $d = 3$ nm, the leg volume can be estimated as $V \approx 1.7 \times 10^{-19}$ cm^3. The estimates obtained for the number of states per unit volume by Eq. (2) are given in Table 1. The given estimates for the density of states per unit volume correspond to nearly 1.4 electrons in the tip half of the tetrapod leg. The central part of the tetrapod with consideration for four legs contains nearly three electrons at such dimensions. The electron liquid and such low numbers of electrons imply the inner tetrapod charge associated with certain carriers. The charge density concentration per unit length can be estimated as follows:

$$\frac{dN_e}{dz} = 0.001 \text{ nm}^{-1}. \tag{12}$$

The summary electron charge in the tetrapod of $Q_e = 1e$–$3e$ was used for numerical calculations.

3.2. Appendix 2. Estimating the Density of States

The density of lateral quantum modes without consideration for spin can be estimated on the basis of a two-dimensional rectangular potential square well with a base surface area S equal to the surface area of a leg cross section. The estimated density of laterally quantum tetrapod modes is

$$\frac{dn_\perp}{dE} = \frac{2m^*S}{\pi\hbar^2}. \tag{13}$$

where m^* is the effective mass of the electrons. The number of laterally quantum modes between the chemical potentials of the substrate and the STM needle per unit applied bias voltage can be estimated as

$$\frac{\Delta n_\perp}{\Delta V_T} = \frac{dn_\perp}{dE}e = \frac{2m^*Se}{\pi\hbar^2}. \tag{14}$$

For a tetrapod with a transverse leg size of 4 nm, this parameter is $\Delta n_\perp \sim 5$ V^{-1}.

The number of longitudinal states within the range from the energy of a laterally quantum mode to the chemical potential of the STM needle of substrate on every laterally quantum mode with consideration for spin can also be estimated from the potential square well model as

$$\Delta n_{\|}(n_{\perp}, V_T) = \Theta(E_{n_{\perp}} + eV_T - E_c) \times \frac{2L}{\hbar\pi}\sqrt{2m^*(E_{n_{\perp}} + \eta eV_T - E_c)}, \tag{15}$$

where $\Theta(...)$ is the Heaviside function, E_c is the conduction band bottom of a tetrapod leg, which is definitely different for the different legs, but may be taken for estimation as a certain averaged characteristic, and η is the output voltage ratio governed by the geometry of a tetrapod and tunneling barriers and the position of the conduction band bottom inside the tetrapod. The number of longitudinal states on one lateral mode within a voltage range of 1 V for one tetrapod leg with a characteristic length of 50 nm is $\Delta n_{\|} \sim 40$.

3.3. Appendix 3. Correction for the Real Geometry of a Tetrapod

Let us further consider the quasi-one-dimensional model of a tetrapod with three legs. Let the branching point be denoted as z_b. Let two tetrapod legs on the left of this point be labeled by the indices $(l, 1)$ and $(l, 2)$, and the leg on the right of this point be labeled with r.

Since Kirchhoff's law will be true in real experiment for the sum of currents at the branching point, it should be expected that the density of probability currents at the branching point must also satisfy the analogue of Kirchhoff's law

$$j_{l,1}(z_b) + j_{l,2}(z_b) = j_r(z_b). \tag{16}$$

This equation will be fulfilled if the first derivative of the wave function meets the requirement of continuity on the left and right in the form

$$\left.\frac{\partial\Psi_{l,1}(z)}{\partial z}\right|_{z=z_b} + \left.\frac{\partial\Psi_{l,2}(z)}{\partial z}\right|_{z=z_b} = \left.\frac{\partial\Psi_r(z)}{\partial z}\right|_{z=z_b}. \tag{17}$$

As the tetrapod, as assumed, has a symmetric structure, the condition

$$\left.\frac{\partial\Psi_{l,1}(z)}{\partial z}\right|_{z=z_b} + \left.\frac{\partial\Psi_{l,2}(z)}{\partial z}\right|_{z=z_b} = \frac{1}{2}\left.\frac{\partial\Psi_r(z)}{\partial z}\right|_{z=z_b}. \tag{18}$$

must be fulfilled.

The probability density distribution must be continuous at the branching point, as there are no physical factors that could result in the formation of its jump. Hence, the wave function must also change in a continuous manner. From this fact it follows that the wave function must satisfy the following condition:

$$\Psi_{l,1}(z)|_{z=z_b} = \Psi_{l,2}(z)|_{z=z_b} = \frac{1}{2}\partial\Psi_r(z)|_{z=z_b}. \tag{19}$$

Using all the above, the boundary conditions for the transition from the left tetrapod leg with the index "1" into the right leg can be written in the matrix form

$$\begin{pmatrix}\Psi_r^+(z_b)\\ \Psi_r^-(z_b)\end{pmatrix} = \begin{pmatrix}\dfrac{k_r + k_{l,1}}{k_r} & \dfrac{k_r - k_{l,1}}{k_r}\\ \dfrac{k_r - k_{l,1}}{k_r} & \dfrac{k_r + k_{l,1}}{k_r}\end{pmatrix}\begin{pmatrix}\Psi_{l,1}^+(z_b)\\ \Psi_{l,1}^-(z_b)\end{pmatrix}. \tag{20}$$

Denoting the probability of transmission through the leg with an index "1"and "2" as T_1 and T_2, respectively, and the probability of reflection as $\mathcal{R}$, we write the normalization condition as

$$T_1 + T_2 + R = 1. \tag{21}$$

By defining these probabilities in a standard fashion as the ratio between the inlet and outlet fluxes, it is possible to assume that the probability of transmission through such a structure is equal to $2T_1$.

The similar normalization condition for the backward process can be written as

$$\mathcal{R}_1 + \mathcal{R}_2 + T = 1. \tag{22}$$

ACKNOWLEDGMENTS

This work was financially supported by the Russian Foundation for Basic Research (grant no. 16-52-12031 NNIO_a) and the Russian Scientific Foundation (grant no. 16-12-00072).

REFERENCES

1. D. V. Talapin, J.-S. Lee, M. V. Kovalenko, and E. V. Shevchenko, Chem. Rev. **110**, 389 (2010).
2. X. Lan, S. Masala, and E. H. Sargent, Nat. Mater. **13**, 233 (2014).
3. F. Hetsch, N. Zhao, S. V. Kershaw, and A. L. Rogach, Mater. Today **16**, 312 (2013).
4. Y. Shirasaki, G. J. Supran, M. G. Bawendi, and V. Bulovic, Nat. Photonics **7**, 13 (2013).
5. R. B. Vasiliev, D. N. Dirin, and A. M. Gaskov, Russ. Chem. Rev. **80**, 1139 (2011). https://doi.org/10.1070/RC2011v080n12ABEH004240
6. L. Manna, E. C. Scher, and A. P. Alivisatos, J. Am. Chem. Soc. **122**, 12700 (2000).
7. M. Kuno, O. Ahmad, V. Protasenko, D. Bacinello, and T. H. Kosel, Chem. Mater. **18**, 5722 (2006).
8. S. Ithurria and B. Dubertret, J. Am. Chem. Soc. **130**, 16504 (2008).
9. S. Ithurria et al., Nat. Mater. **10**, 936 (2011).
10. N. N. Schlenskaya et al., Chem. Mater. **29**, 579 (2017).
11. R. B. Vasiliev et al., Chem. Mater. **30**, 1710 (2018).
12. W. U. Huynh, X. Peng, and A. P. Alivisatos, Proc. Electrochem. Soc. **99**, 11 (1999).
13. B. Sun, E. Marx, and N. C. Greenham, Nano Lett. **3**, 961 (2003).
14. H. Wang et al., J. Mater. Chem. **22**, 12532 (2012).

15. L. Manna, D. J. Milliron, A. Meisel, E. C. Scher, and A. P. Alivisatos, Nat. Mater. **2**, 382 (2003).
16. D. J. Milliron et al., Nature **430**, 190 (2004).
17. S. Deka et al., Nano Lett. **10**, 3770 (2010).
18. A. G. Kanaras, C. Sönnichsen, H. Liu, and A. P. Alivisatos, Nano Lett. **5**, 2164 (2005).
19. Y. Cui, U. Banin, M. T. Björk, and A. P. Alivisatos, Nano Lett. **5**, 1519 (2005).
20. R. B. Vasiliev et al., J. Mater. Res. **26**, 1621 (2011).
21. A. Trifonov et al., Radioengineering **35**, 40 (2013).
22. I. Gur, N. A. Fromer, and A. P. Alivisatos, J. Phys. Chem. B **110**, 25543 (2006).
23. H. Steinberg et al., Nano Lett. **9**, 3671 (2009).
24. H. Steinberg et al., Nano Lett. **10**, 2416 (2010).
25. C. Canali, F. Nava, G. Ottaviani, and C. Paorici, Solid State Commun. **11**, 105 (1972).
26. K. Sattler, *Handbook of Nanophysics: Nanoparticles and Quantum Dots* (CRC Press, 2010).
27. S. Sze, *Physics of Semiconductor Devices* (Wiley, 1981).
28. A. Harwit, J. S. Harris, and A. Kapitulnik, J. Appl. Phys. **60**, 3211 (1986).
29. R. Tsu and L. Esaki, Appl. Phys. Lett. **22**, 562 (1973).
30. H. Liu, Superlattices Microstruct. **3**, 379 (1987).
31. M. Jonson and A. Grincwajg, Appl. Phys. Lett. **51**, 1729 (1987).
32. L. Fang et al., J. Chem. Phys. **127**, 184704 (2007).
33. S. Yamada, J. Phys. Soc. Jpn. **15**, 1940 (1960).

Translated by E. Glushachenkova

SPELL: 1. schematized